Stockholm University

Bachelor Thesis

Degree Project in
Geological Sciences, 15 hp

Conglomerate clasts and subduction-related Cretaceous arc volcanism

Anton Klaman

Stockholm 2026

Department of Geological Sciences
Stockholm University
SE-106 91 Stockholm

Acknowledgements

I want to express my sincere gratitude to my supervisor, Victoria Pease, for her guidance, support, and valuable feedback throughout this thesis project. I am also grateful to Alasdair Skelton for sharing his knowledge and perspectives, which have inspired me throughout the programme. I would also like to thank Elisabeth Däcker for her assistance and support during my studies.

Finally, I would like to thank my friends and family for their encouragement, patience and support.

Thank you to everyone who have supported me along the way.

Abstract

Geochemical analyses of conglomeratic volcanic clasts from Koyukuk basin, Alaska, constrain magma genesis and evolution, and relate samples to regional tectonics. Major and trace element data are mostly sub-alkaline and felsic, defining predominately calc-alkaline differentiation trends. Enrichment in fluid-mobile elements and depletion of immobile high field strength elements suggest subduction-related sources for the volcanic clasts. Sample variations in rare earth element patterns and trace element ratios indicate different depths of melting, degrees of crustal interaction, and fractionation processes control magma evolution. Differences and similarities in geochemical data identify relatively distinct groups of samples, where overlapping ages and characteristics reflect a complex dynamic magmatic open system with a strong subduction signature. The results suggest a progression of tectonic events during the accretion of an intra-oceanic arc against mainland Alaska, ranging from mid-Jurassic to mid-Cretaceous in age.

Table of Contents

1. Introduction

Geochemical analysis of volcanic rocks involves the study of major element oxides and element concentrations. The volcanic rocks of the Koyukuk basin, Alaska, are preserved as clasts in conglomerates. Volcanic clasts from conglomerates in the northern Koyukuk-basin reflect diverse ages and tectonic environments (Fredriksson & Pease, 2022), from subduction-related to mid-ocean ridge-related. Knowing the geochemical signature of the volcanic clasts sampled from conglomerates further to the south will help to better define the source and tectonic settings(s) of these rocks. A suite of forty-five clasts, thin-sections, and major element oxides and element concentration data are used to determine the tectonic setting of these rocks in order to constrain the petrogenesis and tectonic setting of these magmatic clasts.

2. Geological Setting & Background

2.1 The Yukon-Koyukuk Basin

The Koyukuk basin in western Alaska consists of two sub-basins separated by a curved outcrop of early Cretaceous volcanic rocks, that together define a triangular region (Figure 1). The Yukon-Koyukuk basin is bordered by the Brooks Range to the north, the Seaward peninsula to the west, and the Ruby terrane to the east. The continental rocks consist of (i) metasedimentary pelitic schist and carbonate rocks of Paleozoic age, and (ii) mafic volcanic and intrusive rocks of late Paleozoic & early Mesozoic age that also occur as intrusive bodies across the region (Patton Jr., 1973). The sub-basins are known as the Kobuk-Koyukuk basin to the north and the Lower Yukon basin to the South (Figure 1).

The interior of the Yukon-Koyukuk basin exposes early Cretaceous volcanic rocks ranging from mafic to intermediate composition and interpreted to reflect various tectonic settings. They are overlain by late-early Cretaceous marine turbidites that give way to Cretaceous sandstones and conglomerates of fluvial origin (Patton, 1973; Seminara et al., 2024; Till et al., 1993). Patton (1989), quotes... “felsic extrusive and hypabyssal rocks, chiefly... rhyolites, are widespread in the eastern part of the province.”, with an estimated age of late Cretaceous and lower Tertiary. A belt of Cretaceous granitic plutons, dated by the potassium-argon method and known as the Hogatza belt, stretches across the province and is both spatially and temporally related to these late Cretaceous rhyolites (Patton & Box, 1989). There is evidence of thrust-fault contacts between these Cretaceous volcanic rocks and the metasedimentary rocks of Seward Peninsula, as well as the western Brooks Range. There are also folds and faults across the entire province that trend northeast and die out at the Brooks Range fold belt to the north (Patton, 1973). It's a province defined by a volcanic core bound in oceanic crust sutured to continental borderlands and accompanied by marine to terrigenous basin in-filled by sediment (Patton & Box, 1989; Seminara et al., 2024).

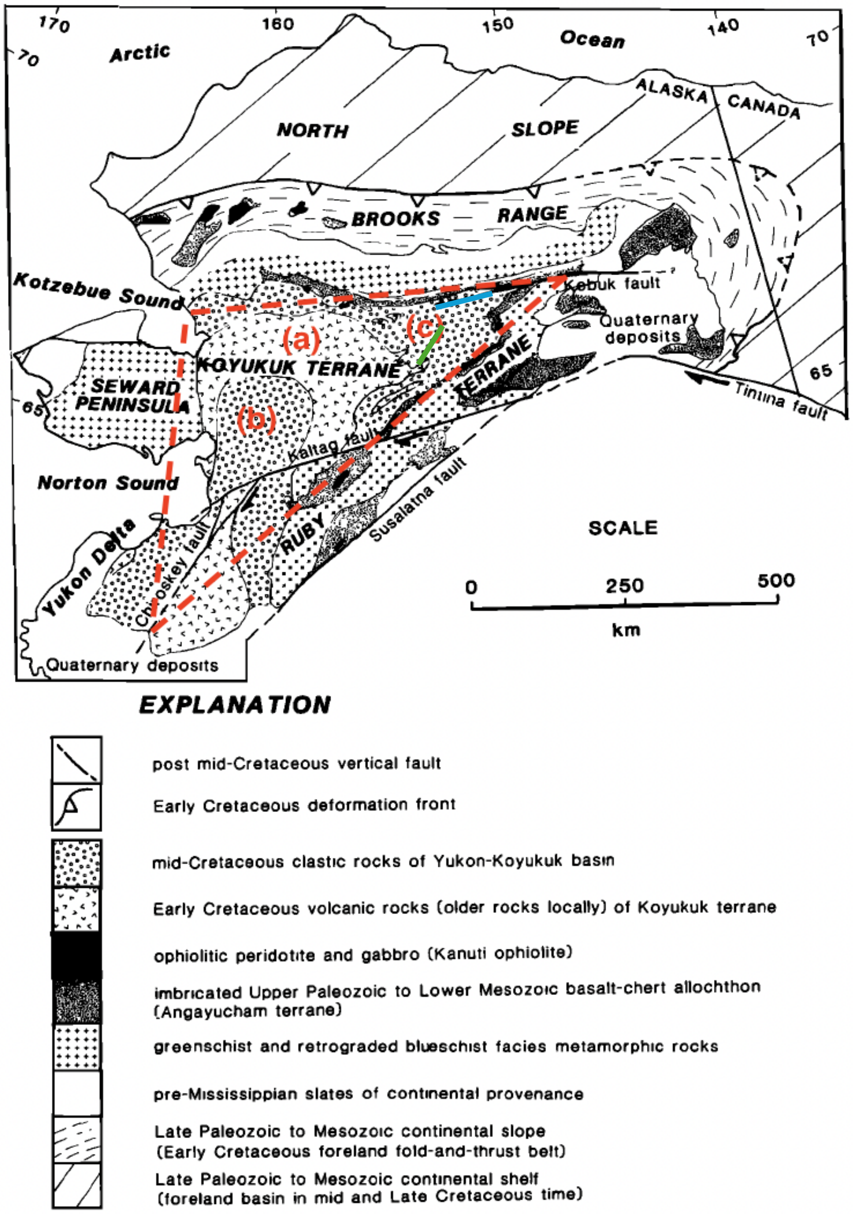

Figure 1. Regional map of study area (red dashed line) with legend. (a) Koyukuk Arc Terrance (KAT), (b) Lower Yukon basin to the south, (c) Kobuk-Koyukuk basin to the north-east (after Patton and Box, 1989). Blue line shows sample traverse of Fredriksson & Pease (2022); green line is the traverse representing samples collected for this study.

2.2 Cretaceous Accretionary Orogeny

The region is partly a product of Cretaceous plate convergence where obduction resulted in parts of the oceanic plate sliding over the continental plate. The obduction process places the lowest oceanic layer above younger units (Patton, 1973; Patton & Box, 1989). The northern Yukon-Koyukuk basin sits on top of the oceanic crust, trapped between the intra-oceanic Koyukuk Arc Terrane (KAT) and the continental borderlands during collision. Blueschist- and greenschist facies metamorphic rocks within the underlying continental plate indicate subduction of the continental margin and is consistent with obduction of the overlying oceanic crust. The time of rifting, formation of the arc, and the subsequent collision of the arc with the continental margin spans approximately the Devonian, mid Jurassic and late Jurassic, respectively (Patton & Box, 1989). The competing interpretations for the formational history of the Yukon-Koyukuk basin suggest that it formed as a fore-arc basin or in an extensional regime after arc collision with the Alaskan margin (Simone et al., 2024; O'Brien et al., 2017; Till et al., 1993; Patton & Box, 1989).

2.3 Geochemistry of Subduction-related Magmatic Rocks

Magma genesis is reflected in rock geochemical composition. Mafic magmas are characterized by high MgO and FeO contents and low SiO_2. MgO and FeO are removed from mafic magmas as the early crystallizing minerals, such as olivine and pyroxene, contain these oxides. The process of 'fractional crystallization' progressively removes mafic phases which also increase the silica and alkalis in the remaining melt, driving magmatic evolution. The subalkaline classification (see Figure 2) includes tholeiitic and calc-alkaline magmatic suites, where the latter typifies subduction related magmatism and an increasingly felsic composition with relatively low Fe-enrichment via crystal fractionation (Kelemen et al., 2003).

Subduction related processes naturally involve fluids derived from dewatering of the subducting slab with increasing depth and temperature. Consequently, rocks from arc magmas are typically enriched in large-ion lithophile elements (LILE) such as Barium (Ba) and Thorium (Th) as they are mobile in a fluid. In contrast, high-field-strength elements (HFSE) are not fluid mobile and thus remain in the subducting slab which means that arc magmas are depleted in trace elements such as Niobium (Nb) (Kelemen et al., 2003). This 'decoupling' in the behavior of the incompatible LIL and HFS elements, which should behave similarly but do not, is known as the subduction zone signature.

3. Methods

3.1 Geochemical dataset

A geochemical dataset for this study was provided for evaluation and consisted of forty-five whole rock analyses of volcanic clasts from conglomerates of the Koyukuk basin. The dataset includes concentrations of the major oxides SiO_2, Al_2O, Fe_2O_3 (total), MnO, CaO, Na_2O, K2O, TiO_2 and P_2O in *wt.%*, along with their respective loss on ignition (LOI) and limits of detection (LOD). Trace elemental abundances in *ppm* with respective LOD were also provided for Ba, Cr, Cs, Cu, Ga, Hf, Nb, Ni, Pb, Rb, Sc, Sr, Ta, Th, U, V, Y, Zr and La, Ce, Pr, Nd, Sm, Eu, Gd, Tb, Dy, Ho, Er, Tm, Yb, Lu. Thin sections were provided for most of the samples. As all analytical measurements and preparation of thin sections were performed prior to this study, those procedural methods will not be described here. Some samples, chiefly the more felsic ones, have been dated by the U-Pb method using zircon.

3.2 Quality assessment and data processing

Analytical totals for the major oxides, including LOI, show good quality as they range from 99% to 101%, which lies within the preferred range of analytical uncertainty and natural deviation. Samples VP22-02, -20, -27, -29, -33, -37, -39, -44 and -45 were outside this range and were thus discarded to maintain data quality. The geochemical data of major oxides were converted to dry-normalized values for graphical representation. Major oxides concentrations below the LOD are treated as half the LOD to minimize inflation of concentration and bias in the data. Elemental data used for logarithmic plotting is handled differently. To minimize large variance, all elements are limited by a static LOD value- chosen to be 0.1 because most of the elements' LOD, and samples that reach this limit, are close to this value. It is important that all rocks analyzed have maintained their original chemistry, otherwise altered samples may skew the results. As such, samples with high LOI or that were outliers (VP22-32) on graphical plots were flagged for potential alteration and their respective thin-sections were evaluated using a petrographic microscope.

3.3 Petrography

Samples required microscopic examination due to the above criteria and were examined to identify the reason for their non-uniform (VP22-32) and representative (VP22-25, -16) behavior and to evaluate typical mineral assemblages and reactions. Petrographic observations were used to support interpretations derived from geochemical analyses, such as confirming expected fractionation and alteration.

3.4 Analytical techniques and geochemical diagrams

Geochemical plots of the dataset were constructed to specifically test for subduction and magmatic arc processes. Major oxides were evaluated with variation diagrams such as *Total alkali vs. Silica* (TAS), *Pearce' Elemental Ratio* (PER) and *Bivariate plots,* as well as the *Alkali-Iron-Magnesium* (AFM) discrimination diagram. Trace elemental data was evaluated using multielement plots, rare earth elemental (REE) plots, and discrimination diagrams.

3.4.1 Major elements

Assigning the samples to a compositional group is done using the TAS diagram (Figure 2). It is made by plotting dry-normalized totals of SiO_2 versus K_2O + Na_2O on the empirically derived whole-rock geochemical compilation (Le Bas et al., 1986 and Le Maître et al., 2002). Distinguishing magmatic differentiation trends allows insight into the genesis, source, and tectonic environment of the samples. This is done with the AFM diagram (Figure 3), which distinguishes the tholeiitic and calc-alkaline magma series using the boundary of Vermeesch & Pease (2021). Samples VP22-08, -22, and -38 appear alkaline and were therefore excluded from the AFM. Bivariate plots are used to represent the geochemistry of the samples. From these, crystal fractional processes may be inferred and further tested. PERs are then used to test for specific fractionating minerals and constrain magmatic evolution, which can identify potential cogenetic relationships between magmas.

3.4.2 Trace elements

As the geological history of the Yukon-Koyukuk basin is known to be partly associated with a subduction zone environment, subduction mobile and immobile elements are of great value in recognizing the subduction zone signature. Rare earth element (REE)- and multi-element diagrams normalized to NMORB are used to visualize geochemical patterns, along with partial melting processes, and subduction related signatures. In the same way, specific element ratios are used to discriminate between different tectonic settings based on how these trace elements are expected to behave. For example, Th, Yb and Nb are used to distinguish samples derived from direct mantle melting versus those derived in magmatic arcs due to their fluid-mobile/immobile behavior.

4. Results

4.1 Total alkali vs. Silica

The data are generally subalkaline, although there are a few alkaline mafic basaltic and intermediate andesitic samples (Figure 2). The data set is dominated by rhyolite samples with SiO2 contents exceeding 70% (Figure 2). Some of the rhyolites have been dated (from 175 to 114 Ma) and these samples are color-coded to more easily identify their geochemical variations. Samples VP22-22 and -38 have high LOI and plot as alkaline, and VP22-08 (not high LOI) straddles the divide, they are therefore excluded from further discussion.

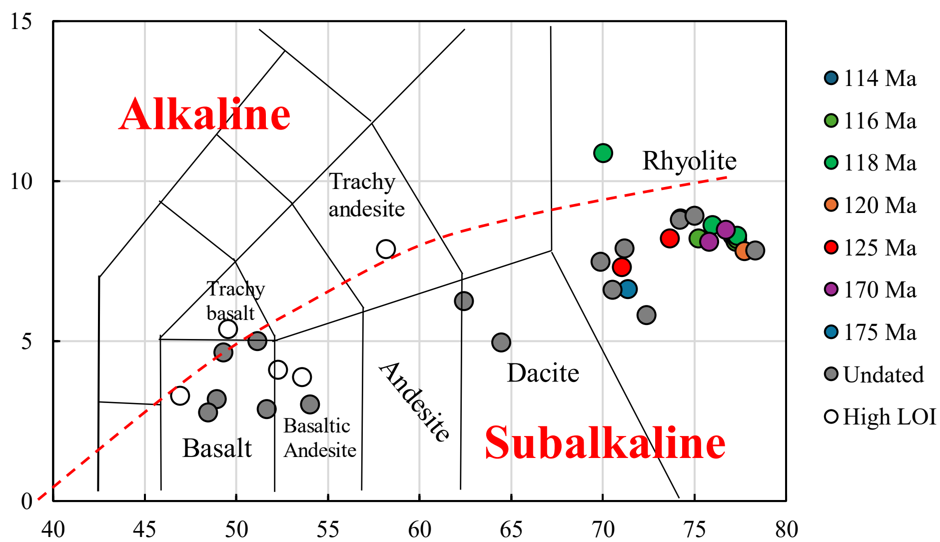

Figure 2. Silica (SiO2) versus total alkalis (K2O + Na2O). Total 36 samples (excluding 9 due to high LOI) are color coded by age. The red line separates samples into alkaline and subalkaline series. Samples are mostly basalt, basaltic andesite, dacite, and rhyolite (after Le Bas et al, 1986).

4.2 Alkali-Iron-Magnesium Diagram (AFM)

All subalkaline samples are plotted on the AFM to distinguish between the tholeiitic and calc-alkaline magma series (Figure 3). Some undated, basaltic to dacitic samples straddle the divide between the tholeiitic and calc-alkaline series, and seem to follow the tholeiitic trend, whereas some samples are calc-alkaline (Figure 3a). The more evolved samples (dacites to rhyolites) follow the typical trend of increasing alkalis with increasing silica content (Figure 3a). Samples of different compositions but of the same age may be related by a common evolutionary pathway, so samples dated 114 Ma, 116 Ma and 118 Ma are joined by color-coded lines (Figure 3b). Three undated samples (VP22-35, -28, -10) lie near the linear array of these age groups (Figure 3b).

4.3 Harker diagrams

Samples of the same age have been plotted together on major oxide bivariate plots (Figure 4). For 114 Ma, this includes samples VP22-04, -05, and -13; for 116 Ma this includes samples VP22-11, -14, -16, and -17; for 118 Ma this includes samples VP22-18, -25, and -32.

4.4 Pearce Elemental Ratio (PERs)

The dated samples forming the 114 Ma, 116 Ma, and 118 Ma age groups are evaluated for minerals expected to fractionate from more evolved magmas, i.e. alkali feldspar, plagioclase, and quartz, using Pearce element ratio (PER) diagrams (Figure 5). Linear regressions of PER plots are summarized in Table 1. The linear regression is considered good if R-squared is > 0.95, and poor if R-squared is < 0.95. The 114 Ma samples define good fits for all tested minerals. The fit remains good when incorporating sample VP22-35, and -10 into the regression, but not as good for VP22-28 are included (Table 1). 116 Ma and 118 Ma show no good fits for any of the undated samples.

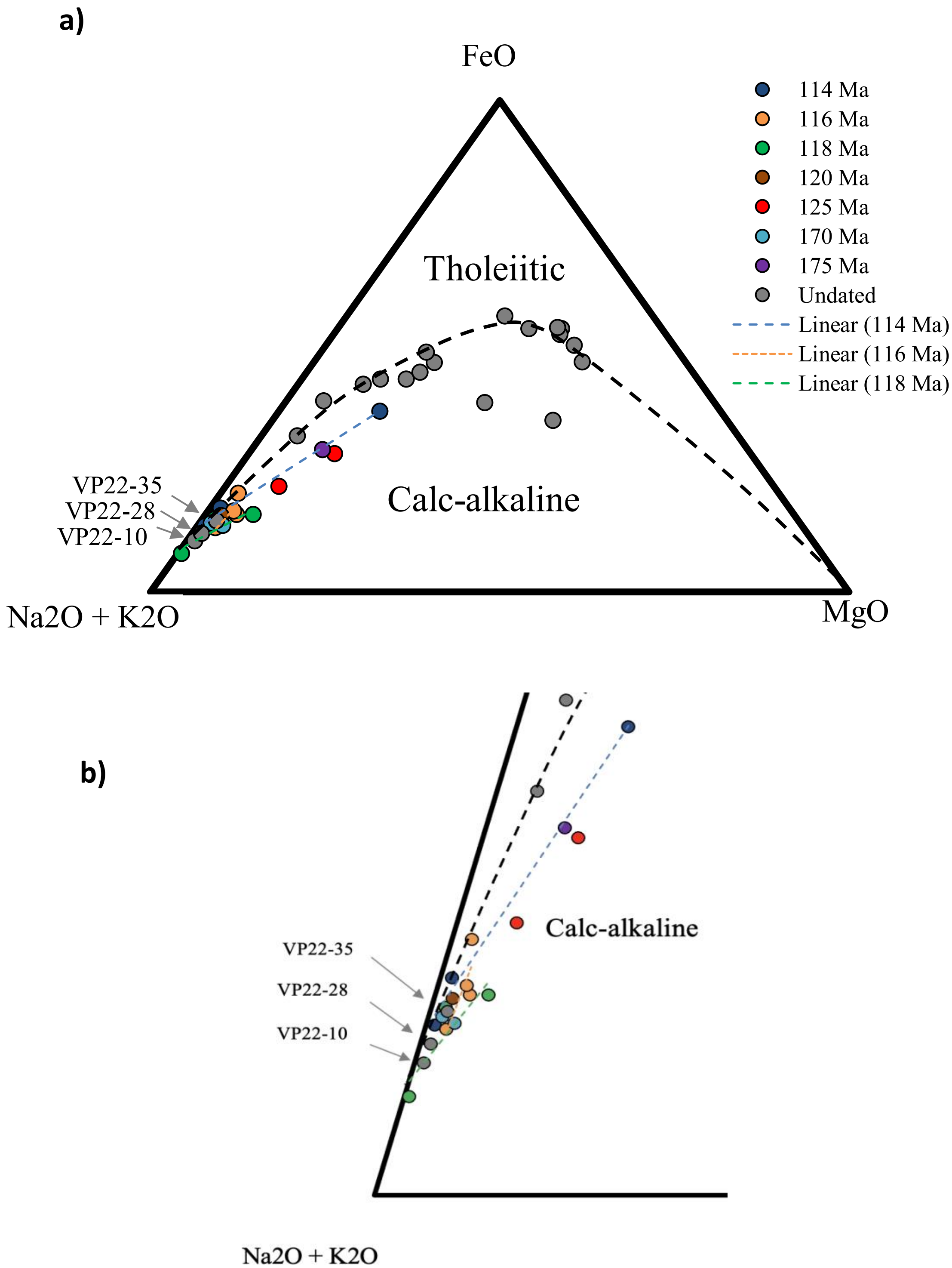

Figure 3. Alkali-Iron-Magnesium (AFM) diagram. (a) The data are mostly calc-alkaline (after Vermeesch & Pease, 2021). (b) Close-up of alkali apex showing inferred evolution of samples with similar ages.

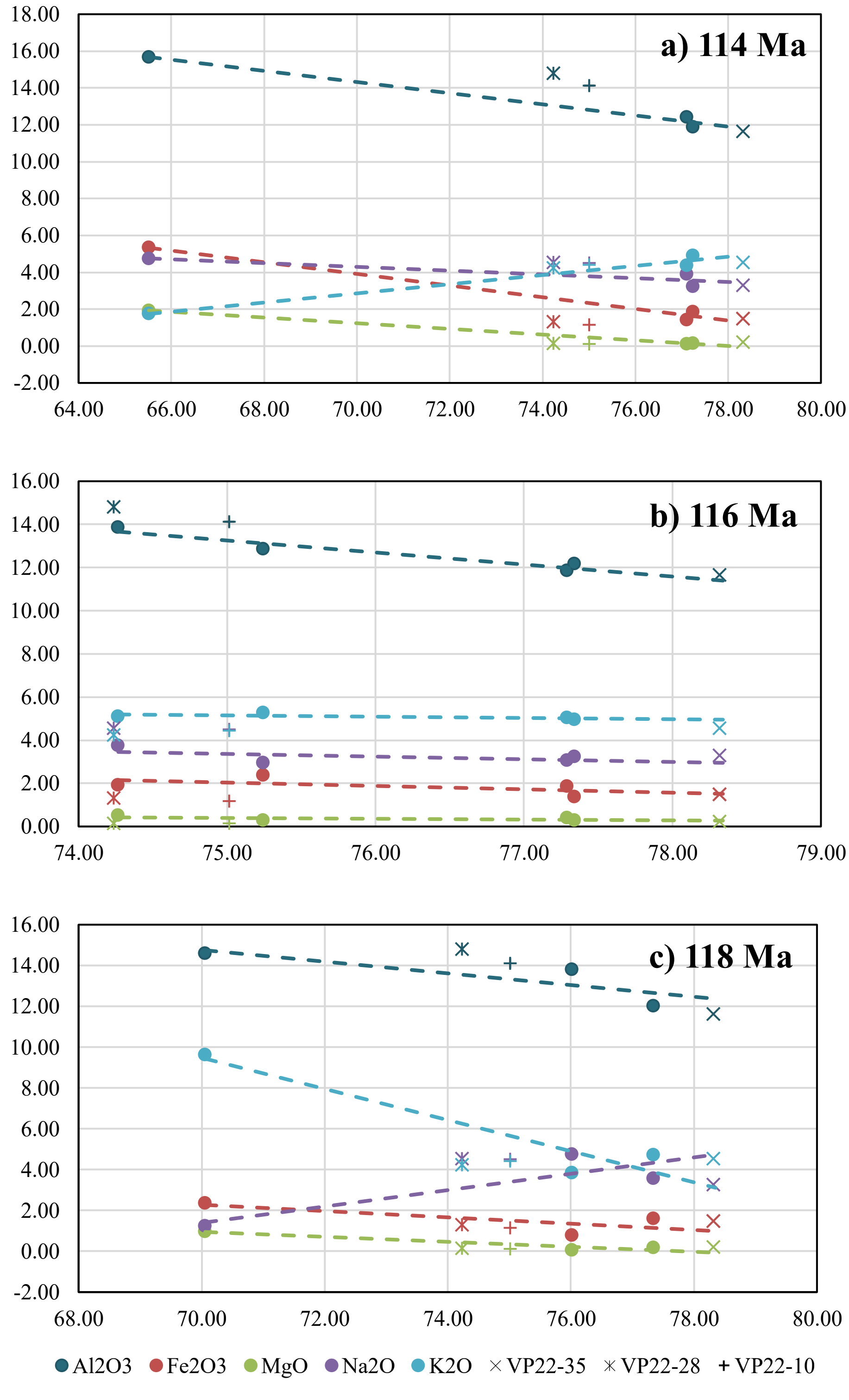

Figure 4. Harker diagrams of major oxides for aged samples belonging to (a) 114 Ma, (b) 116 Ma, (c) 118 Ma, and undated samples VP22-35, VP22-28 and VP22-10.

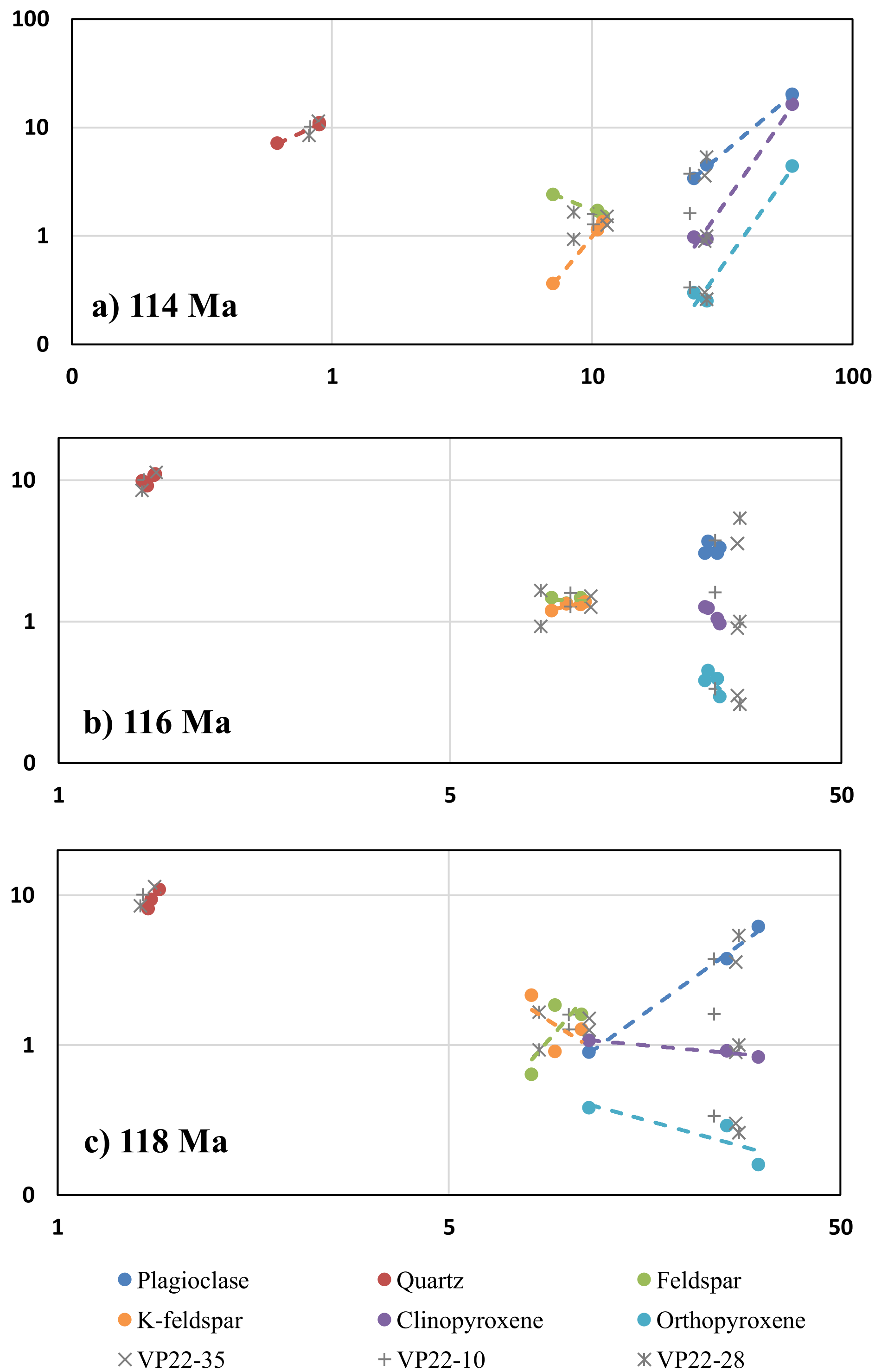

Figure 5. Pearce elemental ratio (PERs) diagrams plotting values of oxides versus each other to evaluate degree of cogenetic magma fractionation history for dated samples (a) 114 Ma, (b) 116 Ma, (c) 118 Ma.

Table 1. Linear regression statistics for dated and undated samples [1]

		Plg	Qtz	Feldspar	Ksp	Cpx	Opx
114 Ma	**R-squared**	1.00	0.98	0.99	0.99	0.99	0.99
	VP22-35	1.00	0.95	0.99	0.98	0.99	0.99
	VP22-28	1.00	0.88	0.71	0.93	0.99	0.99
	VP22-10	1.00	0.98	0.96	0.95	0.98	0.99
116 Ma	**R-squared**	0.01	0.58	0.02	0.81	0.98	0.42
	VP22-35	0.14	0.67	0.07	0.32	0.84	0.53
	VP22-28	0.74	0.71	0.46	0.79	0.57	0.68
	VP22-10	0.00	0.49	0.02	0.80	0.13	0.43
118 Ma	**R-squared**	0.96	0.96	0.49	0.39	0.99	0.87
	VP22-35	0.89	0.71	0.38	0.33	0.99	0.74
	VP22-28	0.95	0.75	0.26	0.12	0.68	0.84
	VP22-10	0.96	0.20	0.51	0.40	0.05	0.75

Notes: 1, Values >0.95 are considered a good fit (green); red color indicates a poor fit.

Plg, plagioclase; Qtz, quartz; Ksp, potassium feldspar; Cpx, clinopyroxene; Opx, orthopyroxene.

4.5 Multi-element & Rare Earth Element Graphs & Elemental Ratios

Normalized multi-element and rare earth element graphs are shown in figure 6. The basalts have generally flat multi-element pattern with negative Nb anomalies ($[Nb/Nb^*)_N$ = 0.009 – 0.048]; where [$Nb^* = \sqrt{La*Th}$]) and depletion of Nb relative to La and Th ($[Nb/La]_N$ = 0.01 – 0.09; $[Nb/Th]_N$ = 0.006 – 0.05) (Figure 6a). One basaltic andesite is similar to the basalts ($[Nb/Nb^*]_N$ = 0.015; $[Nb/La]_N$ = 0.02; $[Nb/Th]_N$ = 0.009), the other two are depleted in Nb relative to La and Th ($[Nb/La]_N$ = 0.05 – 0.8); $[Nb/Th]_N$ = 0.009 – 0.2). The Andesite sample has the highest concentrations of trace elements and no significant Nb or Eu anomalies ($[Nb/Nb^*]_N$ = 0.87; $[Eu/Eu^*]_N$ = 0.75; where [$Eu^* = \sqrt{Sm*Gd}$]). Two rhyolite types are defined, one type with negative Eu- and Nb anomalies ($[Eu/Eu^*]_N$ = 0.05 – 0.28; $[Nb/Nb^*]_N$ = 0.09 – 0.24) and one without negative Eu ($[Eu/Eu^*]_N \approx 0.8$; ($[Nb/Nb^*]_N \approx 0.17$). Some rhyolites with negative Eu don't define negative Nb ($[Nb/Nb^*]_N$ = 0.62 – 0.89), including samples VP22-10, -28, and a sample dated to 116 Ma (VP22-11). Most rhyolites define a depletion of Nb relative to La and Th ($[Nb/La]_N$ = 0.27

– 0.88); $[Nb/Th]_N$ = 0.013 – 0.03). Some samples are less depleted in Nb relative to Th ([Nb/Th]N = 0.12 – 0.22) and more enriched in Nb relative to La ([Nb/La]N = 3 – 6.1), VP22-10, -28, and a sample dated to 116 Ma (VP22-11) are one of those.

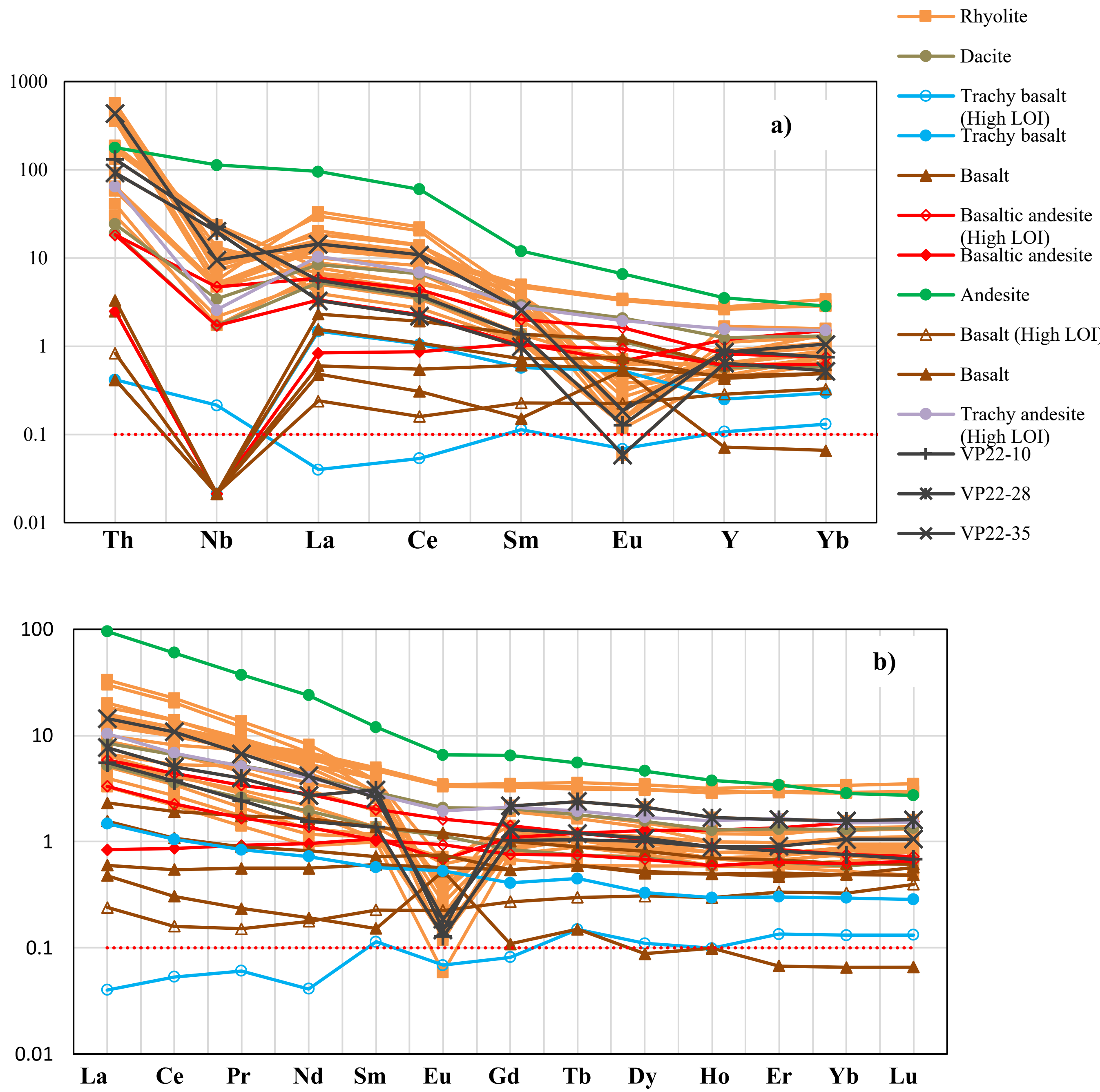

Figure 6. (a) Multi-element and (b) rare earth element diagram showing immobile trace elemental abundances for the suite of rocks from Yukon-Koyukuk basin area, normalized to N-MORB values by Sun and McDonough (1989).

All samples have decreasing LREE from La through Nd (Figure 6b), with the exception of some basalts $[La/Nd]_N$ = 1 – 1.9; $[La/Yb]_N$ = 0.7 – 7.3) and one basaltic andesite $[La/Nd]_N$ = 0.88; $[La/Yb]_N$ = 0.55). One basalt has decreasing LREE and a positive Eu-anomaly ($[La/Nd]_N$ = 2.5; $[Eu/Eu^*]_N$ = 4.1). Rhyolites with negative Eu anomalies have decreasing LREE $[La/Nd]_N$ = 1.9 – 4.35 [La/Yb] = 4.8 – 50.1), as do rhyolites without a significant Eu anomaly $[La/Nd]_N$ = 2– 3.4; [La/Yb] = 4.2 – 11). Most samples have flat HREE: the basalts ($[Dy/Yb]_N$ = 0.8 – 1.4; $[Ho/Lu]_N$ = 0.75 – 1.5), the rhyolitic samples with anomalies ($[Dy/Yb]_N$ = 0.88 – 1.4; $[Ho/Lu]_N$ = 0.8 – 1.3) and the rhyolitic samples without anomalies ($[Dy/Yb]_N$ = 1; $[Ho/Lu]_N$ = 0.9 – 1). To summarize, most samples lack fractionated HREEs, while the basaltic samples have flat overall REE patterns, whereas the andesitic to rhyolitic samples have enriched LREE patterns and the andesite sample, and the basalt with positive Eu-anomaly, have fractionated HREE.

4.6 Elemental Ratios

Although all basalt samples have very low Nb (below the LOD), most samples reveal pronounced negative Nb anomalies (0.015 – 0.87). The degree of Nb-depletion is quantified by the Nb/Nb* ratio which represents the value of Nb relative to neighboring element La and Th. Low Nb ratios are a signature of volcanic arcs and identify subduction related sources. Nb is less fluid mobile than La, and Th with increasing depth and temperature, so Nb is retained within the subducting slab in residual mineral phases such as rutile. This results in an enrichment of La and Th relative to Nb, as reflected in the Nb/Th and Nb/La ratios. Therefore, low Nb/La (0.27 – 0.88) and Nb/Th (0.013 – 0.03 for most rhyolites) ratios reflect the presence of fluids derived from the slab (Fredriksson & Pease, 2022) and subducted terrigenous sediments (Kelemen & Hanghoj & Greene, 2003), respectively. High amounts of Th may also suggest involvement of continental crust in magma genesis, consistent with findings of Miller (1989).

Similarly to Nb/Nb*, the Eu/Eu* ratio quantifies the value of Eu relative to its neighboring elements Sm and Gd. Our data defined two types of rhyolites- one with low Eu/Eu*, i.e.- negative anomaly of 0.05 – 0.28; this indicates that plagioclase was likely a strongly fractionating phase (Moll-Stalcup & Arth, 1989). This is because Eu is compatible in plagioclase which results in a removal of Eu when plagioclase fractionates, and this is reflected in low Eu/Eu* ratios (Kelemen & Hanghoj & Greene, 2003).

These samples have relatively flat HREE ratios of Ho/Lu = 0.8 – 1.3 and Dy/Yb = 0.8 – 1.4. The ratio of HREE like Ho/Lu and Dy/Yb constrain source depth and are consistent with a shallow spinel-bearing mantle source (Fredriksson & Pease, 2022). One andesite and one basalt exhibit weakly depleting HREE patterns suggesting minor HREE fractionation, possibly a transition from a garnet stability field or minor amounts of garnet present in a mostly spinel-bearing mantle. In contrast, the ratio of La/Nd tracks the fractionation degree of the LREE. The rhyolites exhibit pronounced enrichment and fractionation of the LREE with La/Nd ratios of 2 – 4 times NMORB values. The ratio of La/Yb, where both are incompatible but La is more incompatible, represents the relative enrichment between LREE and HREE. Most of the samples have moderate enrichment of La/Yb ≈ 7, which together with flat Dy/Yb ratios indicate absence of depletion by residual garnet, and instead reflect an enriched mantle source by subduction derived components, or modest crustal contamination.

4.7 Petrography

Two samples from 118 Ma (VP22-25, -32), and one from 116 Ma (VP22-16) were looked at due to their representative nature and alkaline composition. Their LOI and analytical totals lie within acceptable range. The singular alkaline rhyolitic sample belonging to 118 Ma (VP22-25) shows clear hydrothermal alteration (Figure 7b), indicated by cloudy textures that reflect microscopic imperfections caused by intruding alkali rich fluids. As subduction signatures are heavily dependent on fluid-immobile Nb, the sample is still considered relevant despite being alkaline and will be used for interpretation. All samples exhibit typical mineralogy expected of highly evolved felsic samples. The 116 Ma sample differs from the 118 Ma sample with its interlocking crystals and phaneritic texture, reflecting slower cooling and a plutonic history.

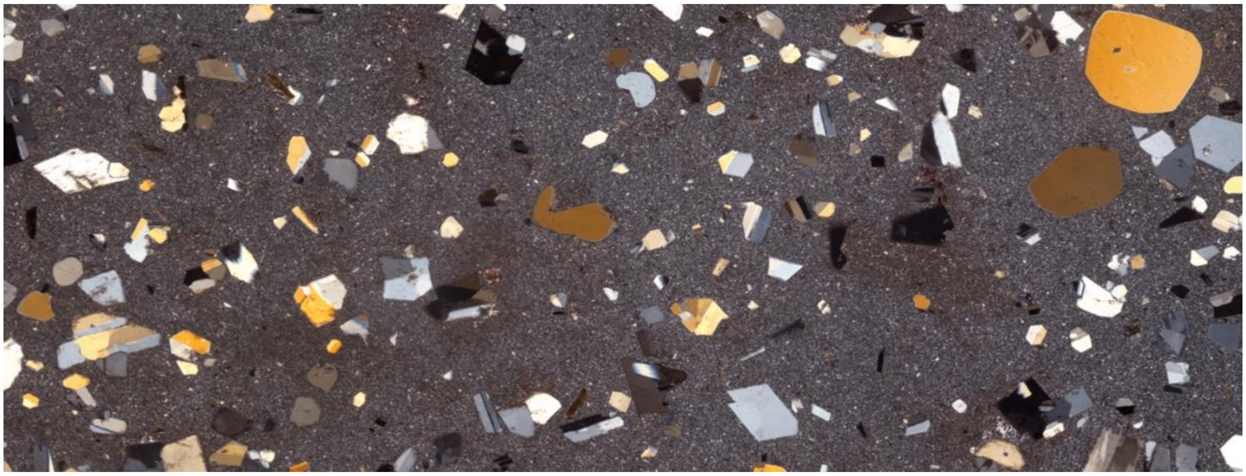

(a)

(b)

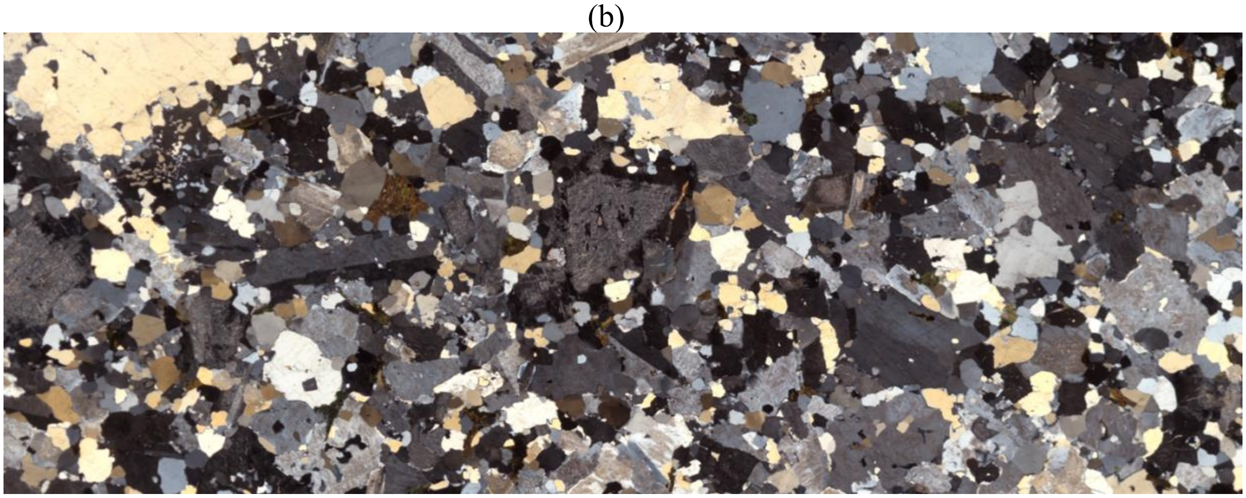

(c)

Figure 7. Thin section microphotographs of volcanic clasts collected for this study. Clasts: (a) VP22-25 of 118 Ma, subalkaline, porphyritic texture (rapid cooling history) and euhedral minerals of plagioclase, pyroxene, quartz, feldspar, and without alteration; (b) VP22-32 of 118 Ma, alkaline with porphyritic texture (slower cooling than VP22-25) and subhedral minerals of plagioclase, minor pyroxene, quartz, feldspar, and with alteration; (c) VP22-16 of 116 Ma, subalkaline with phaneritic texture (slow cooling history) and minerals of plagioclase, pyroxene, quartz, feldspar, and without alteration.

5. Discussion

5.1 Age correlations

The dated samples of 114 Ma, 116 Ma and 118 Ma appear to define an evolutionary path in the AFM diagram (Figure 3). Based on these three dated suites, undated sample VP22-35 lies on the 114 Ma trend and may reasonably be attributed to it, while undated samples VP22-28 and VP22-10 lie near the 116 - 118 Ma suites and may tentatively be correlated with them. Linear regression statistics of the PER plots (Table 1) indicate that VP22-35 is a very good fit for the 114 Ma suite ($R^2 > 0.95$) across all tested minerals.

To further evaluate these possible correlations, the undated samples have been plotted separately with multi-element and REEs (Figures 7 and 8). Although VP22-28 and VP22-10 are poorer fits in the PER modelling compared to VP22-35, their multi-element (Figure 8) and REE patterns (Figure 9) fit well within the framework of the dated suites. VP22-10, and 28, closely resemble the 118 Ma suite with their consistent Th and absence of a pronounced Nb anomaly, as well as similar enrichment and depletion patterns for multielement and REE. VP22-10, and -28 display enrichment and depletion patterns that are almost identical to those of 116 Ma. However, they differ in that 116 Ma has a more pronounced Nb anomaly and higher Th. VP22-28 has slightly higher concentration of HREE than the other samples (Figure 6b), although its relative enrichment and depletions trends closely resemble those of the 118 Ma, while appearing slightly more evolved. However, VP22-10 and VP22-28 don't share the 114 Ma Nb depletion and have lower Th, similarly to how they don't match with 116 Ma. VP22-35 displays trace-element patterns that are nearly identical to samples of the 114 Ma suite.

The similarity in relative enrichment and depletion trends of VP22-35 and the 114 Ma suite, together with the strong cogenetic potential and genetic relationship defined in the PER and bivariate plots, support the interpretation that VP22-35 belongs to the 114 Ma suite. In contrast, there is no equally strong evidence for a cogenetic relationship between VP22-28 and VP22-10 based on the PER and bivariate plots, making their inferred age correlations weaker. However, both samples display REE and multi-element patterns that are nearly identical to those of VP22-11 (116 Ma) and VP22-25 (118 Ma), respectively, supporting their correlation with both age groups. Rhyolite samples lacking a significant negative Eu anomaly share Th-enrichment and Yb-depletion characteristics with the rhyolite sample dated to 175 Ma, suggesting that they may belong to that group.

5.2 Mantle source

The N-MORB normalized REE ratios of the basaltic samples are approximately 1 or below (Figure 6b), reflecting a variably depleted, shallow, non-garnet-bearing mantle source. A positive Eu anomaly in one basaltic sample may indicate a shallow, plagioclase-bearing mantle. The evolved andesitic to rhyolitic samples are enriched in LREE while displaying relatively flat N-MORB normalized HREEs of approximately 1 (Figure 6b), which is also consistent with shallow mantle source.

The suite shows clear subduction-related input on tectonic discrimination diagrams. All samples plot within the arc array (Figure 10) and the mafic samples segregate into intra-oceanic and continental arc types (Figure 11). The compositions of magmas within the arc array reflect input of slab derived fluid and melts enriched in incompatible elements, resulting in enrichment of the mantle wedge. Of the mafic samples, the less evolved basalts plot as ‘forearc & intra-arc’, while the increasingly evolved samples document more continental influence. The shift into continental signature is a result of a transition of the magma, probably caused by interaction with continental crust or subducted sediments, reflected in increased ratios of La/Yb and Th/Nb (Patton & Box, 1989).

The andesitic-rhyolitic samples Th and Nb relative to Yb clearly represent an arc-array involving greater continental geochemical signatures (Figure 10). The absence of any andesitic to rhyolitic samples plotting outside the subduction-related field further strengthens the interpretation of a subduction tectonic setting. Th and Nb concentrations of the basaltic samples define them as intra-oceanic arc related rather than MORB-like, while also displaying a continental arc magmatism affinity (Figure 11). This transitional character is consistent with the evolution of an intra-oceanic arcs evolution into a continental volcanic arc.

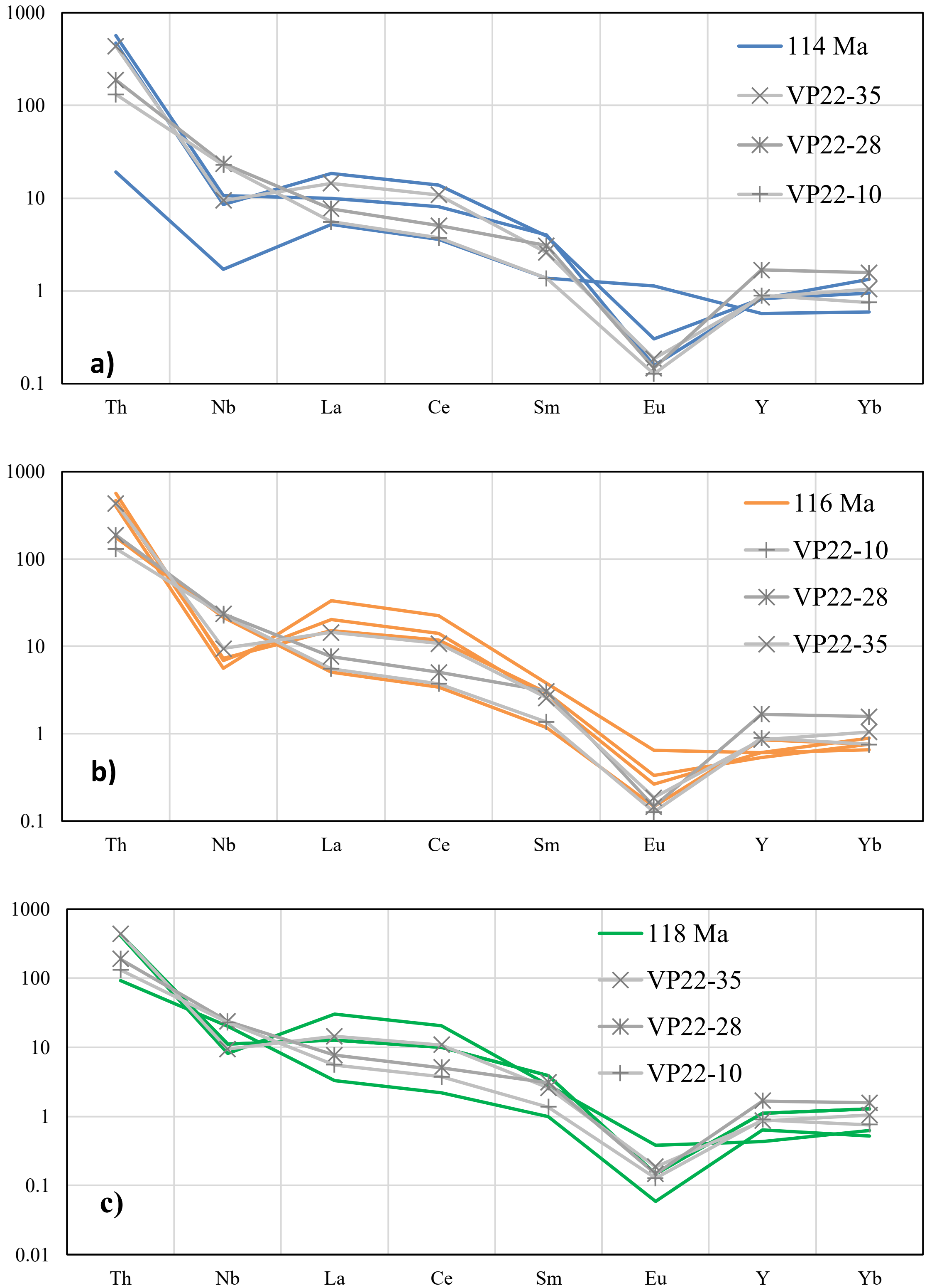

Figure 8. Multielement diagrams of the dated samples (a) 114 Ma, (b) 116 Ma, (c) 118 ma- with select undated samples to visualize a geochemical evolutionary fit.

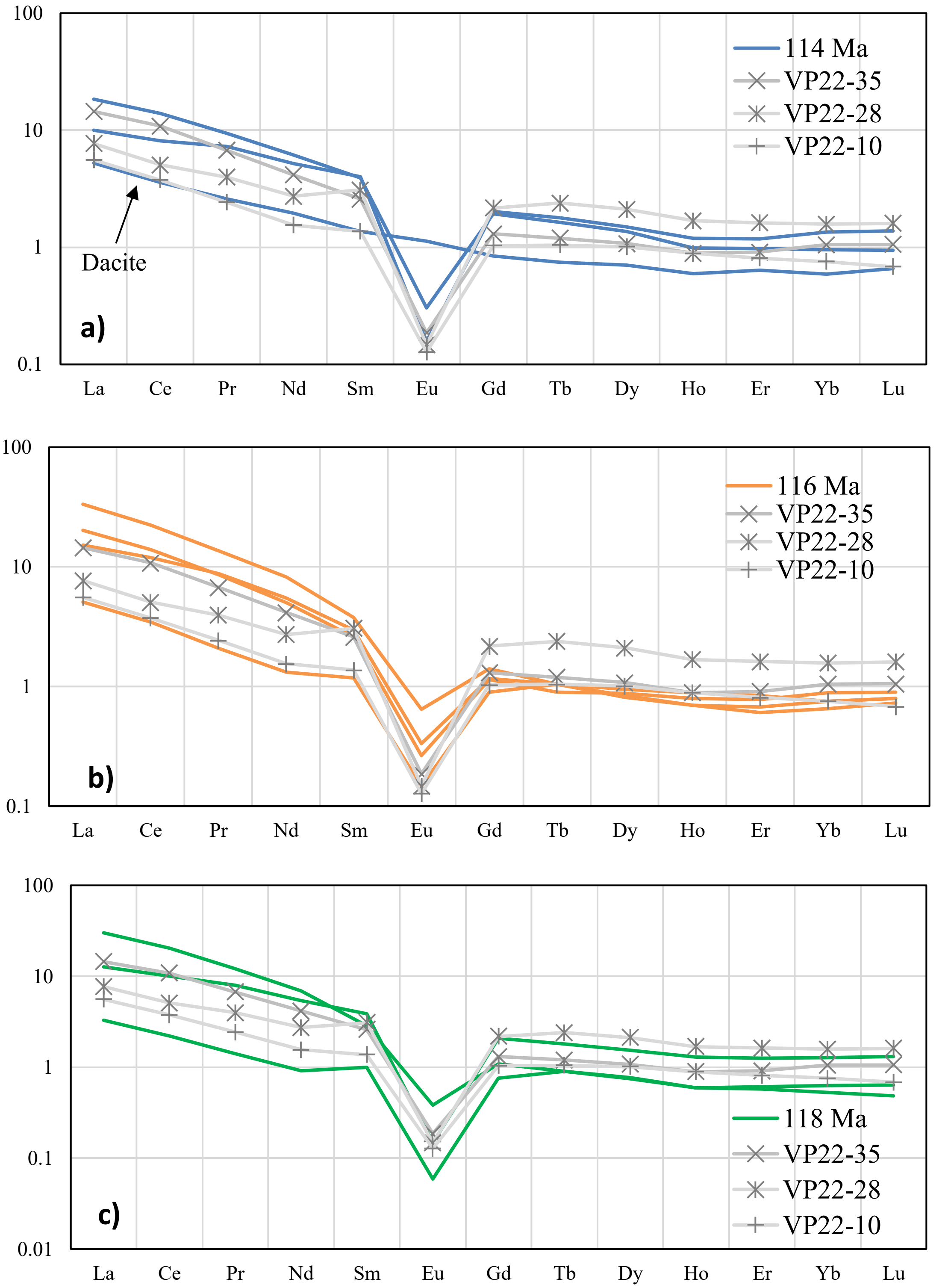

Figure 9. Rare earth element diagrams of the dated samples (a) 114 Ma, (b) 116 Ma, (c) 118 Ma- with select undated samples to visualize geochemical evolutionary fit.

Variation in Eu anomalies within the rhyolitic samples suggest differing melting and fractionation conditions, consistent with the observed cooling history and minerals present in 116 Ma and 118 Ma thin sections (Figure 7). The rhyolites displaying negative Eu anomalies likely reflect significant plagioclase fractionation and/or melting within plagioclase stability field, consistent with shallow mantle source. In contrast, rhyolites lacking significant Eu anomalies exhibit comparatively weaker Th-enrichment relative to HFSE and Nb, which may indicate a source with a lower subduction-related input and/or comparatively higher degrees of crustal contamination.

5.3 Magma genesis

The geochemical data indicate that the samples from Koyukuk basin are mostly evolved subalkaline rocks that display alkali enrichment without prior iron enrichment (Figures 2 and 3), which is characteristic of a calc-alkaline magmatism in subduction-related settings. Calc-alkaline magmas are typically formed in conjunction to subduction zones as the fluids expelled from the subducting slab metasomatizes the overlying wedge. This causes early saturation and fractionation of Fe-Ti oxides, producing the typical Calc-alkaline trend (Fredriksson & Pease, 2022).

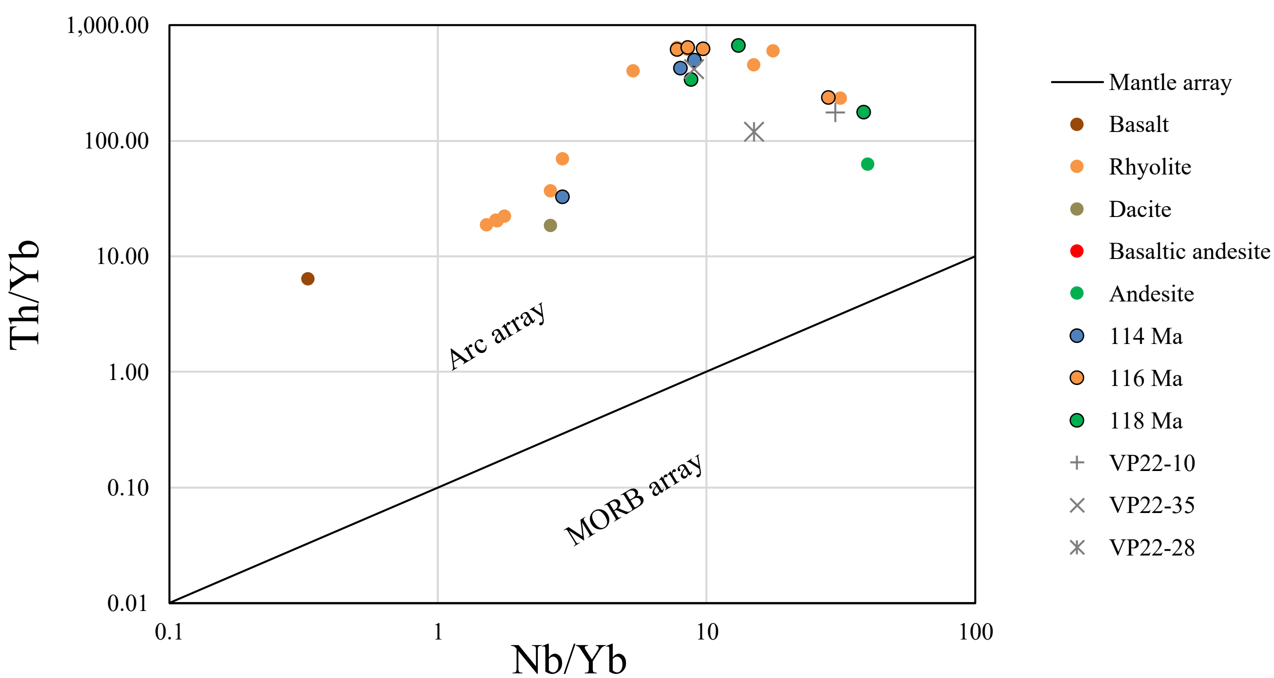

Figure 10. Logarithmic elemental ratios Th/Yb vs. Nb/Yb expressed in ppm that indicate source of the sample by discriminating volcanic arc and MORB source (after Pearce, 1984, 2008).

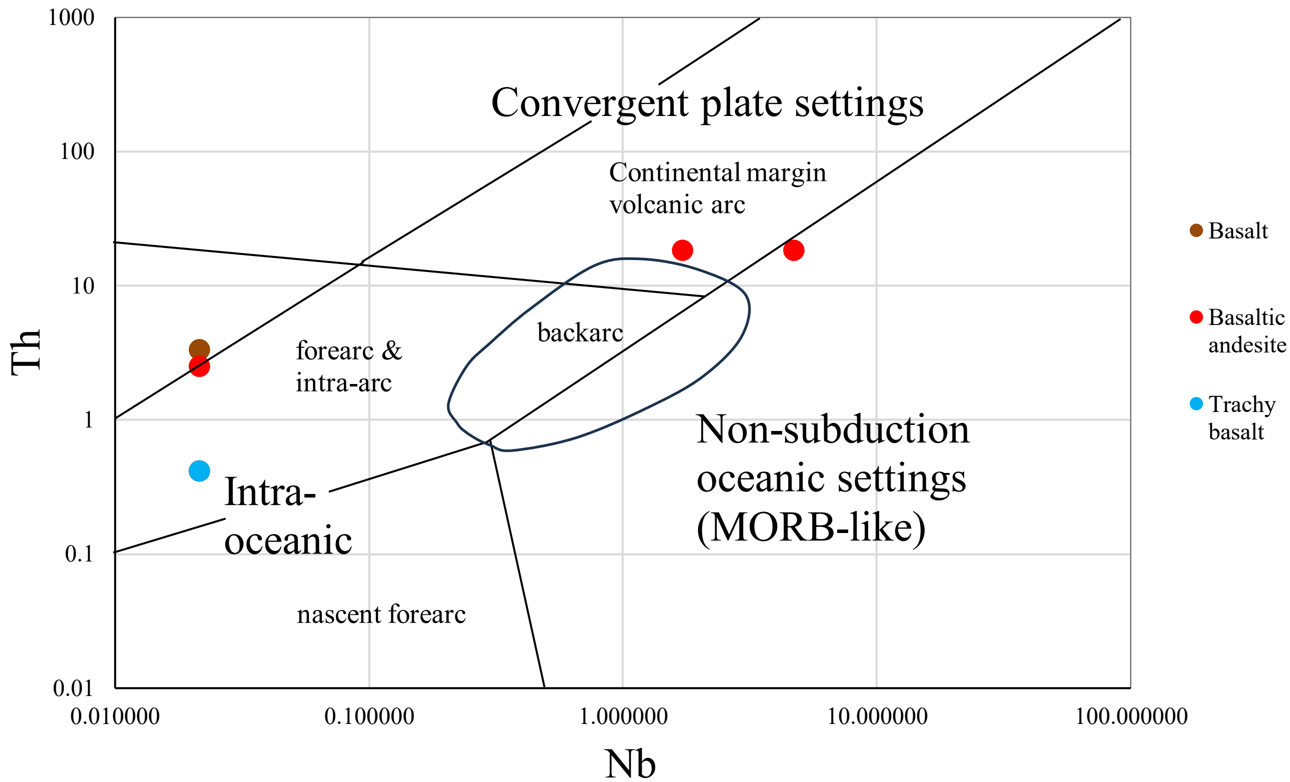

Figure 11. Discrimination diagram for tectonic setting signatures for elemental abundances Th & Nb for mafic samples according to Roberto Saccini (2015), plotted on a logarithmic scale, normalized to N-MORB values of Sun and McDonough (1989).

The Harker diagrams define the progressive decrease in major oxides expected during magma evolution through fractional crystallization (Figure 4), and is consistent with the crystallization of clinopyroxene, potassium feldspar, plagioclase, and quartz as indicated by the PER diagrams (Figure 5 and Table 1). It is also consistent with negative Eu anomalies signifying plagioclase removal (Figure 6b), and the presence of them in thin sections of 116 Ma and 118 Ma (Figure 7).

Most basalts and andesitic to rhyolitic samples share Th enrichment and Nb depletion. This geochemical signature is characteristic of subduction-related magmatism because Nb is fluid-immobile and remains in the residual slab while fluid-mobile elements like Th are transferred into the mantle wedge during slab dehydration, producing Th-enrichment and Nb-depletion in arc magmas.

Undated samples VP22-10 and VP22-28 both display relatively high Nb/Th and Nb/La ratios, consistent with VP22-11 of the 116 Ma suite and VP22-25 of the 118 Ma suite. Elevated Nb/Th ratios may indicate comparatively weak crustal assimilation and/or reduced subduction input developed from relatively shallow mantle depths where slab-fluid contributions are diminished and magma ascends relatively fast. This group also defines comparatively lower La/Yb and Th/Yb ratios relative to the rhyolites with pronounced negative Eu anomalies. These lower ratios suggest limited crustal assimilation, and a depth where plagioclase formation was suppressed, consistent with shallow conditions. The relatively high Nb concentrations relative to Th suggests formation proximal to a subduction-related setting where Nb depletion was less pronounced.

6. Conclusions

Geochemical data from the volcanic clasts of the Koyukuk Basin indicate that they are predominantly subalkaline, calc-alkaline magmas generated in a subduction-related tectonic setting. Major-element trends, REE- and multi-element patterns, and tectonic discrimination diagrams collectively support derivation from a mantle wedge metasomatized by slab-derived fluids during slab dehydration and resulting in arc magmatism. The decoupling of incompatible elements (enrichment of fluid-mobile elements and depletion of HFSE), defines a clear subduction signature. Both the basaltic- and andesitic to rhyolitic samples reflect melting of a shallow, non-garnet bearing source, where the latter record varying degrees of crustal interaction.

Major oxide trends and PER modelling suggest that samples VP22-35 correlates best with the 114 Ma suite. Its consistent evolutionary trends on the AFM and bivariate and strong regression statistics, together with almost identical REE and multi-element patterns, support a strong cogenetic relationship with the 114 Ma suite. VP22-10 and VP22-28 are more tentatively correlated with the 116 Ma and 118 Ma suites, respectively. Although their PER regressions and major oxide trends are weak, the multi-element and REE patterns of VP22-11 and VP22-25 are almost identical to 116 Ma and 118 Ma, respectively, suggesting that they could have formed in the same magmatic subduction systems.

Three relatively distinct groups of rhyolites can be identified from the geochemical dataset. The first group is characterized by strong subduction input, elevated crustal assimilation (or terrigenous sediment), high Th/Yb ratios, and pronounced negative Eu anomalies, suggesting plagioclase fractionation at shallow levels while having comparatively deeper melting conditions. The second group, represented by VP22-10 and VP22-28 together with samples from the 116 – 118 Ma suite (VP22-11 and VP22-25, respectively) record significantly higher Nb/Th and Nb/La ratios together with lower La/Yb and Th/Yb ratios. These represent shallower magma evolution, less crustal assimilation, and a reduced subduction-related signature. These conditions may reflect magma generation and ascent during an extensional regime where rapid magma ascent limits crustal assimilation and slab-rollback reduces subduction-component input. The third rhyolitic group is attributed to 175 Ma and lacks significant Eu anomalies, yet defines shallow melting conditions and record significantly reduced crustal assimilation and Nb enrichment relative to Th - this suggests drier melting conditions and suppression of plagioclase fractionation.

The temporal and tectonic evolution of the dataset is loosely consistent with the formational model of the region proposed by Patton & Box (1989). The 175 Ma sample and geochemically similar undated samples may represent magmatism associated with the early phases of the formation of the Koyukuk Arc Terrane during the mid-Jurassic, which is expected to have dryer conditions as the mantle wedge is not yet heavily metasomatized by slab fluids. In contrast, the younger 118-114 Ma suites record continued magmatism after the collision of the oceanic arc with the continent during the late Jurassic facilitated by a subduction polarity reversal. Overall, the dataset supports the interpretation of the Koyukuk Arc Terrane being the product of an intra-oceanic arc colliding with continental Alaska, reflected in basaltic samples with intra-oceanic signatures and a loose progression of temporally linked samples from 175 Ma – 114 Ma that represent early subduction- and post collisional phases, respectively.

7. References

Fredriksson, C. & Pease, V. (2022) Complex Late Triassic-Middle Jurassic Subduction-Related Magmatic History from Detritus of Nominal Middle Jurassic Brooks Range Ophiolite, Northern Alaska: https://doi.org/10.2113/2022/9601288

Kelemen, P.B. & Hanghoj, K. & Greene, A.R. (2003) One View of the Geochemistry of Subduction-Related Magmatic Arcs, with an Emphasis on Primitive Andesite and Lower Crust: *https://doi.org/10.1016/B0-08-043751-6/03035-8*

Les Bas, M. J. & Le Maitre, R. W. & Streckeisen, A. & Zanetitin, B. (1986) A Chemical Classification of Volcanic Rocks Based on the Total Alkali-Silica Diagram: https://doi.org/10.1093/petrology/27.3.745

Moll-Stalcup, **E. & Arth, J., G.** (1989) The nature of the crust in the Yukon-Koyukuk Province as inferred from the chemical and isotopic composition of five Late Cretaceous to Early Tertiary volcanic fields in western Alaska: https://doi.org/10.1029/JB094iB11p15989

Moll-Stalcup, **E. & Arth, J., G.** (1991) Isotopic and chemical constraints on the petrogenesis of Blackburn Hills volcanic field, western Alaska: https://doi.org/10.1016/0016-7037(91)90073-E

O'Brien, T.M. & Miller, E.L & Pease, V. (2017) Provenance, U-Pb detrital zircon geochronology, Hf isotopic analyses, and Cr-spinel geochemistry of the northeast Yukon-Koyukuk Basin: Implications for interior basin development and sedimentation in Alaska: https://doi.org/10.1130/B31825.1

Seminara, S. & Pease, V. & Toro, J. & Omna, J. et al. (2024) Provenance studies and basin evolution: Insight from the Yukon-Koyukuk basin: https://doi.org/10.1111/sed.13248

Sun, S.-s. & McDonough, W.F. (1989) Chemical and isotopic systematics of oceanic basalts: implications for mantle composition and processes: https://doi.org/10.1144/GSL.SP.1989.042.01.19

Miller, P., Thomas. (1989) Contrasting plutonic rock suites of the Yukon-Koyukuk Basin and the Ruby geanticline, Alaska: https://doi.org/10.1029/JB094iB11p15969

Till, A.B. & Box, S.E. & Roeske, S.M. & Patton Jr., W. (1993) Mid-Cretaceous extensional fragmentation of a Jurassic-early cretaceous compressional orogen, Alaska: https://doi.org/10.1029/91TC00044

William, W. & Patton Jr., W. (1973) Reconnaissance Geology of Northern Yukon-Koyukuk Province, Alaska: https://doi.org/10.3133/pp774A

William, W., Patton Jr., W. & Box, S.E. (1989) Igneous History of the Koyukuk Terrance, Western Alaska: Constraints of the Origin, Evolution, and Ultimate Collision of an Accreted Island Arc Terrace: https://doi.org/10.1029/JB094iB11p15843

William, W., Patton Jr., W. & Box, S.E. (1989) Tectonic Setting of the Yukon-Koyukuk Basin and Its Borderlands, Western Alaska: https://doi.org/10.1029/JB094iB11p15807

Zheng, Y.-f. & Hermann, J. (2014) Geochemistry of continental subduction-zone fluids: https://doi.org/10.1186/1880-5981-66-93

8. Appendix

Table 2. Major oxides in wt.% (including LOI and analytical totals) of all forty-five volcanic clast samples collected for this study.

Sample	SiO2	Al2O3	Fe2O3(T)	MnO	MgO	CaO	Na2O	K2O	TiO2	P2O5	LOI	Wet Total
VP22-01	49.97	22.72	6.19	0.095	4.26	8.91	3.11	1.76	0.492	0.12	2.8	100.4
VP22-02	71.1	13.52	2.54	0.034	0.65	1.39	2.66	5.12	0.381	0.1	0.91	98.4
VP22-03	47.42	18.35	10.95	0.229	6.05	10.8	2.14	0.55	0.96	0.36	1.88	99.7
VP22-04	64.12	15.34	5.22	0.104	1.89	3.87	4.65	1.71	0.725	0.24	1.55	99.4
VP22-05	76.15	11.7	1.84	0.033	0.15	0.55	3.18	4.84	0.12	0.01	0.54	99.1
VP22-06	51.58	13.89	11.21	0.212	5.38	8.04	3.32	0.4	1.96	0.23	3.94	100.2
VP22-07	50.38	17.47	11.17	0.194	4.23	7.84	2.98	0.95	0.906	0.2	4.19	100.5
VP22-08	48.4	26.43	5.14	0.068	1.64	11.47	3.28	1.26	0.408	0.05	2.36	100.5
VP22-09	74.45	12.48	1.41	0.024	0.35	1.37	3.03	4.91	0.132	0.01	0.72	98.9
VP22-10	74.9	14.09	1.16	0.08	0.12	0.53	4.49	4.41	0.038	0.03	0.33	100.2
VP22-11	73.1	13.63	1.87	0.07	0.49	0.52	3.67	5.02	0.038	0.02	0.78	99.2
VP22-12	75.74	12.38	1.52	0.022	0.18	0.43	3.68	4.67	0.047	0.01	0.63	99.3
VP22-13	76.17	12.28	1.4	0.027	0.11	0.55	3.85	4.32	0.063	< 0.01	0.65	99.4
VP22-14	77.41	11.88	1.86	0.023	0.38	0.38	3.07	5.03	0.09	0.03	0.71	100.9
VP22-15	69.61	13.54	3.66	0.056	1.48	1.91	4.29	2.85	0.436	0.12	2.74	100.7
VP22-16	75.01	12.81	2.35	0.044	0.27	0.78	2.92	5.25	0.215	0.04	0.67	100.4
VP22-17	75.8	11.91	1.35	0.019	0.27	0.55	3.15	4.86	0.095	< 0.01	0.78	98.8
VP22-18	75.75	11.77	1.56	0.022	0.18	0.46	3.49	4.62	0.073	< 0.01	0.85	98.8
VP22-19	62.26	13.99	6.64	0.088	2.3	4.61	4.72	0.06	1.33	0.55	2.41	99.0

VP22-20	62.69	13.93	6.22	0.127	2.71	1.72	5.01	1.72	0.841	0.25	3.28	98.5
VP22-21	53.14	15.88	11.13	0.23	6.34	8.09	1.64	1.31	0.504	0.03	2.55	100.8
VP22-22	47.07	21.03	7.55	0.163	8.26	5.68	1.19	3.91	0.087	< 0.01	5.71	100.7
VP22-23	71.65	13.47	2.6	0.092	0.87	0.54	3.59	4.38	0.043	0.02	1.26	98.5
VP22-24	43.7	18.47	11.45	0.196	6.47	9.39	1.04	2.01	0.362	< 0.01	7.44	100.5
VP22-25	75.14	13.65	0.79	0.083	0.06	0.58	4.7	3.81	0.013	0.01	0.67	99.5
VP22-26	59.99	14.19	8.63	0.092	2.53	2.96	4.54	1.45	1.45	0.21	2.56	98.6
VP22-27	53.32	15.81	9.04	0.161	8.01	7.72	0.74	2.3	0.263	0.02	3.58	101.0
VP22-28	72.67	14.48	1.28	0.085	0.14	0.59	4.45	4.14	0.042	0.01	0.63	98.5
VP22-29	44.26	20.42	11.8	0.166	6.34	6.25	0.63	3.78	0.759	< 0.01	3.78	98.2
VP22-30	47.11	16.38	11.57	0.224	7.67	9.45	1.57	1.49	0.73	0.07	2.83	99.1
VP22-31	51.52	16.51	10.05	0.197	7.46	10.38	2.34	0.51	0.595	0.09	1.21	100.9
VP22-32	67.64	14.1	2.29	0.029	0.94	0.85	1.2	9.29	0.19	0.02	1.91	98.5
VP22-33	59.44	14.79	9.04	0.132	2.2	2.46	6.36	0.07	0.78	0.13	3.23	98.6
VP22-34	70.62	14.3	3.41	0.065	1.1	2.41	3.91	2.63	0.366	0.1	1.47	100.4
VP22-35	76.58	11.38	1.44	0.027	0.21	0.39	3.21	4.44	0.092	0.01	0.85	98.6
VP22-36	76.82	11.94	1.59	0.028	0.23	0.35	3.28	4.42	0.106	0.02	0.8	99.6
VP22-37	66.64	10.78	5.28	0.077	1.92	2.06	3.93	1.37	1.045	0.21	5.5	98.8
VP22-38	54.89	15.36	8.88	0.192	3.11	2.83	4.24	3.17	1.395	0.24	5.43	99.7
VP22-39	73.13	11.24	4.83	0.054	0.68	0.43	5.74	0.15	0.407	0.09	1.71	98.5
VP22-40	69.84	14.28	4.24	0.083	0.64	0.65	7.66	0.07	0.494	0.1	1.42	99.5
VP22-41	68.97	13.24	6.11	0.098	1.25	1.01	6.11	0.33	0.519	0.11	2.46	100.2
VP22-42	70.48	12.26	5.83	0.117	1.41	0.98	5.5	0.15	0.497	0.11	2.02	99.4

VP22-43	67.7	13.86	5.43	0.106	0.7	1.2	6.07	1.16	0.509	0.12	2.3	99.2
VP22-44	67	12.91	6.28	0.105	1.02	1.18	4.75	2.62	0.481	0.13	2.33	98.8
VP22-45	66.21	13.62	5.72	0.132	0.6	1.4	5.15	2.57	0.508	0.11	2.28	98.3
LOD	*0.01*	*0.01*	*0.01*	*0.005*	*0.01*	*0.01*	*0.01*	*0.01*	*0.001*	*0.01*		*0.01*

Table 3. Trace element data in ppm, that were used (including LOD) for all forty-five volcanic clast samples collected for this study.

Sample	La	Ce	Pr	Nd	Sm	Eu	Gd	Tb	Dy	Ho	Er	Y	Yb	Lu	Th	Nb
VP22-01	3.7	7.9	1.11	5.3	1.5	0.54	1.5	0.3	1.5	0.3	0.9	7	0.9	0.13	0.4	1
VP22-03	5.8	14.4	2.3	12	3.6	1.23	3.7	0.6	3.7	0.7	2	17	1.9	0.28	0.3	< 1
VP22-04	13.1	26.9	3.43	14.2	3.6	1.15	3.1	0.5	3.2	0.6	1.9	16	1.8	0.3	2.3	4
VP22-05	46	104	12.4	44.7	10.3	0.31	7.1	1.1	6.2	1	2.9	23	2.9	0.43	56.6	20
VP22-06	14.7	32.9	4.49	20.4	5.3	1.66	5.2	0.8	4.8	0.9	2.5	23	2.3	0.33	2.2	11
VP22-07	8.3	17	2.2	10	2.7	0.95	2.8	0.5	3.1	0.6	1.9	17	1.9	0.3	1	4
VP22-08	1.2	2.3	0.31	1.4	0.4	0.54	0.4	< 0.1	0.4	< 0.1	0.2	2	0.2	0.03	< 0.1	< 1
VP22-09	22.1	50	6.02	22.3	5.1	0.44	3.7	0.6	4	0.7	2.2	18	2.7	0.41	42.8	11
VP22-10	13.9	28.1	3.2	11.3	3.6	0.13	3.8	0.7	4.6	0.9	2.4	25	2.3	0.31	15.8	53
VP22-11	12.7	25.8	2.76	9.6	3.1	0.15	3.3	0.7	4.3	0.9	2.5	24	2.3	0.36	21.2	50
VP22-12	16.8	40.1	6.76	25.9	7.2	0.12	4.7	0.7	4	0.7	2	13	2.3	0.38	54	31
VP22-13	25	61.1	9.6	37.7	10.5	0.16	7.4	1.2	6.8	1.2	3.5	23	4.1	0.63	68.1	25
VP22-14	38	89.2	11.6	39.9	7.8	0.34	4.3	0.7	3.7	0.7	2	15	2.3	0.36	56.4	17
VP22-15	13.8	30.6	4.05	15.8	3.6	0.63	3	0.5	3.3	0.7	2.2	18	2.5	0.39	3.6	5

VP22-16	83.4	168	17.9	59.9	9.9	0.66	5.2	0.7	3.8	0.7	1.8	17	2	0.33	48.3	13
VP22-17	50.5	105	11.4	36.5	6.8	0.27	4.2	0.6	4	0.8	2.3	17	2.7	0.41	68	16
VP22-18	31.7	74.9	10.5	39.5	10.2	0.15	7.7	1.2	7	1.3	3.7	31	3.9	0.6	51.8	26
VP22-19	21.1	49.3	6.82	29.5	7.7	2.13	7.5	1.2	7.1	1.3	3.9	35	4	0.61	2.9	8
VP22-21	2.1	6.5	1.22	7	2.8	0.69	4	0.8	5.8	1.3	4	33	4.6	0.7	0.3	< 1
VP22-22	0.1	0.4	0.08	0.3	0.3	0.07	0.3	< 0.1	0.5	0.1	0.4	3	0.4	0.06	< 0.1	< 1
VP22-23	9.9	20.3	2.31	8.6	2.9	0.13	3.1	0.7	4.4	0.8	2.4	24	2.2	0.33	20	53
VP22-24	0.6	1.2	0.2	1.3	0.6	0.23	1	0.2	1.4	0.3	1	8	1	0.18	< 0.1	< 1
VP22-25	8.2	16.5	1.85	6.7	2.6	0.06	2.8	0.6	3.5	0.6	1.7	18	1.6	0.22	11.1	47
VP22-26	239	450	49.2	175	31.5	6.7	23.8	3.7	21.1	3.8	10.2	99	8.7	1.24	21.4	264
VP22-28	19.2	38	5.23	19.9	8.1	0.15	8	1.6	9.6	1.7	4.8	47	4.8	0.73	22.6	55
VP22-30	1.5	4.1	0.74	4.1	1.6	0.58	2	0.4	2.4	0.5	1.5	13	1.5	0.22	< 0.1	< 1
VP22-31	3.9	8.1	1.18	6	1.9	0.76	2	0.4	2.3	0.5	1.4	12	1.5	0.26	0.4	< 1
VP22-32	75.1	153	15.9	50.5	7.5	0.39	4	0.6	3.4	0.6	1.8	12	1.9	0.29	49.5	19
VP22-34	16.2	32.2	3.73	13.6	2.8	0.73	2.5	0.4	2.7	0.6	1.7	16	1.8	0.3	4.9	4
VP22-35	36.1	81.1	8.87	30.3	6.8	0.19	4.8	0.8	4.9	0.9	2.7	24	3.2	0.48	52.3	22
VP22-36	39.7	89.3	9.71	32.3	6.9	0.21	4.9	0.8	5.1	1	2.9	25	3.3	0.51	58.5	19
VP22-38	26	51.4	6.76	29.3	7.3	1.98	7.8	1.3	7.7	1.6	4.9	44	4.6	0.69	7.8	6
VP22-40	36.1	82.2	11.3	50.6	13.1	3.49	12.9	2.4	15.7	3.2	9.8	78	10.4	1.6	7.6	12
VP22-41	33.6	78.3	10.8	47.3	12.4	3.51	12.3	2.2	14	3	8.6	78	8.7	1.33	6.9	11
VP22-42	30.7	73.6	9.81	43.3	12.3	3.42	12.5	2.2	14.3	2.9	8.7	76	8.8	1.33	7.1	11

VP22-43	32.8	77.2	10.3	44.4	12.3	3.37	12.1	2.1	14	2.9	8.9	73	8.9	1.36	7.8	12
LOD	*0.1*	*0.1*	*0.05*	*0.1*	*0.1*	*0.05*	*0.1*	*0.1*	*0.1*	*0.1*	*0.1*	*1*	*0.1*	*0.01*	*0.1*	*1*